Engineering Sciences *Materials*

SOLIDIFICATION

J. A. Dantzig and M. Rappaz

EPFL Press
A Swiss academic publisher distributed by CRC Press

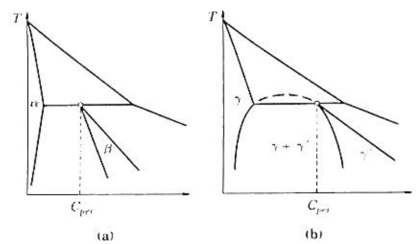

Two peritectic phase diagrams.

Exercise 9.6. Peritectic transformation kinetics.
In Sect. 10.2.2, a solute balance was applied to a peritectic phase diagram in order to deduce the evolution of the $\alpha-\beta$ and $\beta-\ell$ interfaces (Eqs. (10.39) and (10.40)). It was shown that the velocity of the two interfaces, v_α^* and v_β^*, depends in particular on the solute gradient in the peritectic phase, $D_\beta(\partial C_\beta/\partial x)$, taken at each interface. Assume that the solute profile is linear in the β-phase, and show that the expressions for v_α^* and v_β^* become:

$$v_\alpha^* = \frac{dx_\alpha^*}{dt} = \frac{1}{\left(C_\alpha^{*\beta} - C_\beta^{*\alpha}\right)}\left[D_\beta \frac{C_\beta^{*\ell} - C_\beta^{*\alpha}}{x_\beta^* - x_\alpha^*} - D_\alpha \left.\frac{\partial C_\alpha}{\partial x}\right|_{x_\alpha^*}\right]$$

$$v_\beta^* = \frac{dx_\beta^*}{dt} = \frac{1}{\left(C_\beta^{*\ell} - C_\ell^{*\beta}\right)}\left[\frac{dC_\ell^{*\beta}}{dt}\left(\frac{\lambda_2}{2} - x_\beta^*\right) - D_\beta \frac{C_\beta^{*\ell} - C_\beta^{*\alpha}}{x_\beta^* - x_\alpha^*}\right]$$

Neglecting diffusion in the α-phase abd the composition variation in the liquid, integrate these two equations to obtain $x_\alpha^*(t)$ and $x_\beta^*(t)$, and thus the evolution of the thickness of the peritectic phase.

Exercise 9.7. Solidification at low growth rate of a hypoperitectic alloy.
Consider a hypoperitectic alloy of nominal composition $C_\alpha^{per} < C_0 < C_{per}$ with a phase diagram such as the one shown in Fig. 9.25(a). By assuming steady-state and stable α-planar front growth, draw the composition profile in the liquid $C_\ell(z)$, the associated liquidus temperature profiles, $T_{liq}^\alpha(C_\ell(z))$ and $T_{liq}^\beta(C_\ell(z))$, and the actual temperature profile $T(z)$. Do the same for a β-planar front. Show graphically that an undercooled region exists at the solid-liquid interface in both cases.

The cycle illustrated in Fig. 9.26(c) is dependent on the undercooling ΔT_n^α and ΔT_n^β, besides the composition C_0. Fixing ΔT_n^α and ΔT_n^β, what is the range of nominal compositions allowing this cycle to operate?

Exercise 9.8. Solidification at low growth rate of a hyperperitectic alloy.
Consider a hyperperitectic alloy of nominal composition $C_{per} < C_0 < C_\ell^{per}$ with a phase diagram such as the one shown in Fig. 9.25(a) and a stable steady-state β planar front growing at velocity v^* in a thermal gradient G. Draw the composition profile in the liquid $C_\ell(z)$, the associated liquidus temperature profiles $T_{liq}^\beta(C_\ell(z))$ and $T_{liq}^\alpha(C_\ell(z))$, and the actual temperature profile $T(z)$. Show that nucleation of the α phase can take place only in the bulk liquid and not at the $\beta-\ell$ interface. Determine the conditions under which this can occur.

Exercise 9.9. Skewed coupled zone of Al-Si.
Consider the binary Al-Si alloy phase diagram, making the following assumptions for the eutectic invariant and liquidus lines (compositions in wt%, temperatures in °C):

$$T_{liq}^{Al} = 577 - 6.8 \times (C_\ell - 12.2) \quad ; \quad T_{liq}^{Si} = 577 + 9.53 \times (C_\ell - 12.2)$$
$$T_{eut} = 577 \quad ; \quad C_{eut} = 12.2 \tag{9.33}$$

The growth kinetics parameters that appear in Eqs. 9.26 and 9.27 are [20]:

$$A^{Al} = 20\ {}^\circ\mathrm{Cs}^{1/2}\mathrm{mm}^{-1/2} \quad ; \quad A^{Si} = 60\ {}^\circ\mathrm{Cs}^{1/2}\mathrm{mm}^{-1/2}$$
$$A^{eut} = 100\ {}^\circ\mathrm{C}^{3/2}\mathrm{s}^{1/2}\mathrm{mm}^{-1} \tag{9.34}$$

Compute the skewed coupled zone of Al-Si for a thermal gradient G = 10 K/mm and $D_\ell = 3 \times 10^{-3}$ mm²/s. Compare the results with the microstructures shown in Fig. 9.35

9.7 REFERENCES

[1] S. Akamatsu, S. Bottin-Rousseau, and G. Faivre. Experimental evidence for a zigzag bifurcation in bulk lamellar eutectic growth. *Phys. Rev. Lett.*, 93:175701, 2004.
[2] S. Akamatsu, S. Moulinet, and G. Faivre. The formation of lamellar-eutectic grains in thin samples. *Met. Mater. Trans.*, 32A:2039, 2001.
[3] S. Akamatsu, M. Plapp, G. Faivre, and A. Karma. Overstability of lamellar eutectic growth below the minimum-undercooling spacing. *Met. Mater. Trans.*, 35A:1815, 2004.
[4] M. Bobadilla, J. Lacaze, and G. Lesoult. Influence des conditions de solidification sur le déroulement de la solidification des aciers inoxydables austenitiques. *J. Cryst. Growth*, 89:531, 1988.
[5] B. Boettger, V. Witusiewicz, and S. Rex. Phase-field method coupled to Calphad: Quantitative comparison between simulation and experiments in ternary eutectic In-Bi-Sn. In C.-A. Gandin and M. Bellet, editors, *Modeling of Casting, Welding and Advanced Solidification Processes - XI*, page 425, Warrendale, PA, USA, 2006. TMS Publ.
[6] W.J. Boettinger, S.R. Coriell, A.L. Greer, A. Karma, W. Kurz, M. Rappaz, and R. Trivedi. Solidification microstructures: Recent development, future directions. *Acta Mater.*, 48: 43, 2000.
[7] L.F. Donaghey and W.A. Tiller. On the diffusion of solute during the eutectoid and eutectic transformations, Part I. *Mater. Sci. Engrg*, 3:231, 1968/69.
[8] D. D. Double and A. Hellawell. The nucleation and growth of graphite-the modification of cast iron. *Acta Metall. Mater.*, 43 2435, 1995.

velocity (1), a fully coupled eutectic structure is observed. Between (1) and (2), β-dendrites and interdendritic eutectics are expected. Between (2) and (3), a fully coupled eutectic region is found once again, and above velocity (3), α-dendrites with interdendritic eutectics are predicted for this hypereutectic alloy. All together, the resultant coupled zone, where only the eutectic phase is observed, is *skewed* toward the faceted phase, as shown in Fig. 9.34(b).

Unlike regular eutectic systems, it is difficult to predict the skewed coupled zone of an irregular eutectic, since the growth kinetics of both the faceted β-phase and the irregular eutectic cannot be readily quantified. Kurz and Fisher [20] fit the growth kinetics of the faceted α- and non-faceted β-phases with equations of the form:

$$\Delta T^{\alpha} = \frac{GD_\ell}{v^*} + A^{\alpha}\sqrt{v^*} \quad ; \quad \Delta T^{\beta} = \frac{GD_\ell}{v^*} + A^{\beta}\sqrt{v^*} \tag{9.26}$$

with two adjustable parameters A^{α} and A^{β}. The growth kinetics of the eutectic is similar to that given in Eq. (9.18) but also takes into account the influence of the thermal gradient on the growth rate of the irregular eutectic, written as

$$\Delta T^{eut} = A^{eut}\sqrt{\frac{v^*}{G}} \tag{9.27}$$

Exercise 9.9 describes the calculation of the skewed coupled zone for Al-Si binary alloys.

The concept of a skewed coupled zone in a faceted/non-faceted system helps to explain the Al-Si eutectic microstructures shown in Fig. 9.35. In such an alloy solidified at fairly low speed (Fig. 9.35a), a fully eutectic structure is observed. When solidified at higher cooling rate (Fig. 9.35b), a

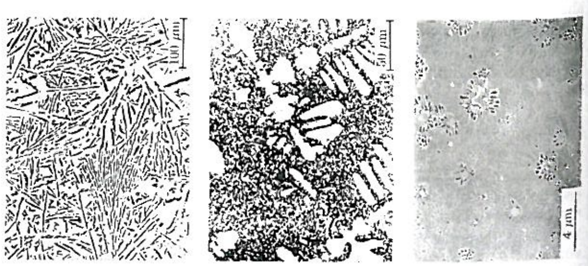

(a) Al-12.5wt%Si (b) Al-12.5wt%Si (c) Al-26wt%Si

Fig. 9.35 Microstructures of various Al-Si alloys: (a) A eutectic composition, slow cooling; (b) A eutectic composition, fast cooling; (c) A hypereutectic composition, laser remelted at 0.1 m s^{-1}. ((a,b) after Hellawell [12], (c) Pierantoni et al. [30].)

few aluminum dendrites form first, before the eutectic, as if the alloy composition was hypoeutectic. Put in the context of the model described above, the corresponding point falls in the $(\alpha + eut)$-region of Fig. 9.34(b). Similarly, for an Al-Si of hypereutectic composition (Fig. 9.35c), a fully eutectic microstructure can be expected if the growth rate is large enough, i.e., if the corresponding point falls in the skewed coupled zone. The micrograph of the laser-solidified alloy remelted at high speed, shows a structure that is slightly more complex. An "equiaxed" structure is formed by nucleation of the silicon phase, as opposed to columnar growth. As the silicon phase grows, the surrounding melt becomes depleted in Si and Al nucleates. It grows as a dendritic microstructure for a short distance, before coupled growth with a very fine lamellar spacing completes the solidification of each grain.

9.5 SUMMARY

The present chapter has demonstrated how two solid phases can grow together in eutectic alloys, such as the foundry alloys Al-Si and cast iron, or the soldering alloys Pb-Sn and Sn-Cu. Near-eutectic composition alloys have a rather narrow solidification interval and are thus easier to cast. The classical theory of Jackson and Hunt for regular lamellar eutectics has been derived in detail, demonstrating how solute exchanges between various phases can contribute to decreasing the required undercooling. This basic theory also facilitates the understanding of the mechanisms involved in the solidification of irregular eutectics, divorced eutectics, eutectic cells and nodular cast iron. Subsequently, peritectic solidification was addressed. Important industrial alloys in this class include bronze and steel. Whereas the peritectic reaction and solidification of the peritectic phase in hypoperitectic alloys occur close to the peritectic temperature, the transformation of the primary α-phase into β is usually incomplete, as it takes place through solid state transformation. Finally, we have seen that the competition of various phases and/or morphologies depends upon the equilibrium phase diagram, but is also strongly influenced by nucleation and growth kinetics. Considering these phenomena, a general criterion for phase selection was identified. The phase or morphology that is observed is the one that has the highest temperature when the velocity is imposed, or the fastest kinetics when the temperature is fixed.

9.6 EXERCISES

Exercise 9.1. Lamellar-fiber transition.
Consider two non-faceted phases α and β having an isotropic interfacial energy $\gamma_{\alpha\beta}$ and forming a regular eutectic. Based on an interfacial energy minimum criterion, calculate the transition volume fraction between fibers